

Article

High-Order Above-Threshold Ionization Using a Bi-Elliptic Orthogonal Two-Color Laser Field with Optimal Field Parameters

Abdulah S. Jašarević ¹, Elvedin Hasović ^{1,*} and Dejan B. Milošević ^{1,2}

¹ Faculty of Science, University of Sarajevo, Zmaja od Bosne 35, 71000 Sarajevo, Bosnia and Herzegovina; abdulah.jasarevic@pmf.unsa.ba (A.S.J.); milo@bih.net.ba (D.B.M.)

² Academy of Sciences and Arts of Bosnia and Herzegovina, Bistrik 7, 71000 Sarajevo, Bosnia and Herzegovina

* Correspondence: elvedin.hasovic@pmf.unsa.ba; Tel.: +387-33279893

Abstract: In the present paper, we study the high-order above-threshold ionization of noble-gas atoms using a bi-elliptic orthogonal two-color (BEOTC) field. We give an overview of the SFA theory and calculate the differential ionization rate for various values of the laser field parameters. We show that the ionization rate strongly depends on the ellipticity and the relative phase between two field components. Using numerical optimization, we find the values of ellipticity and relative phase that maximize the ionization rate at energies close to the cutoff energy. To explain the obtained results, we present, to the best of our knowledge, for the first time the quantum-orbit analysis in the BEOTC field. We find and classify the saddle-point (SP) solutions and study their contributions to the total ionization rate. We analyze quantum orbits and corresponding velocities to explain the contribution of relevant SP solutions.

Keywords: strong-field physics; above-threshold ionization; quantum orbits; saddle-point method



Citation: Jašarević, A.S.; Hasović, E.; Milošević, D.B. High-Order Above-Threshold Ionization Using a Bi-Elliptic Orthogonal Two-Color Laser Field with Optimal Field Parameters. *Atoms* **2023**, *11*, 91. <https://doi.org/10.3390/atoms11060091>

Academic Editor: Yu Hang Lai

Received: 27 April 2023

Revised: 26 May 2023

Accepted: 1 June 2023

Published: 5 June 2023



Copyright: © 2023 by the authors. Licensee MDPI, Basel, Switzerland. This article is an open access article distributed under the terms and conditions of the Creative Commons Attribution (CC BY) license (<https://creativecommons.org/licenses/by/4.0/>).

1. Introduction

The interaction between atoms and molecules with strong tailored laser fields has been an active area of research in recent years due to its potential applications in various fields, including material science and chemistry [1–4]. The ability to manipulate atoms and molecules using laser fields has opened new possibilities for the development of new materials and the study of the fundamental processes of light–matter interaction. The use of strong laser fields also allows the manipulation of electronic and nuclear motion in molecules, which can lead to the formation of new molecular states.

Two of the most interesting atomic and molecular processes induced by strong laser fields are above-threshold ionization (ATI) [5] and high-harmonic generation (HHG) [6]. These processes are usually explained by means of a semiclassical three-step model [7–9]. According to this model, the electron released in tunnel ionization moves, driven by the laser field, and returns to the parent nucleus where it recombines emitting a high harmonic photon in the HHG process or rescatters elastically and is detected with much higher energy in the high-order above-threshold ionization (HATI) process.

In the last decade, it has been possible to study the interaction of atoms and molecules with two-color intense laser fields of different polarizations. One of these fields is the bicircularly polarized field, which consists of two coplanar counter-rotating circular fields with frequencies $r\omega$ and $s\omega$, where r and s are integers. The HHG process by such a counter-rotating bicircular field was first considered almost 30 years ago [10,11]. This phenomenon was initially explained through the strong-field approximation (SFA) and quantum-orbit theory in Ref. [12]. Further investigation of atomic and molecular processes in such fields was triggered by experimental confirmation that the generated high harmonics have circular polarization [13]. In addition to the HHG process, many other strong field processes in

bicircular fields have also been the subject of study. These include above-threshold detachment [14], (H)ATI [15], nonsequential double ionization [16], laser-assisted scattering [17], spin-dependent effects [18], high-harmonic spectroscopy [19], and high harmonics from relativistic plasmas [20].

In addition to the interaction with the bicircular field, strong-field processes in the presence of the orthogonal two-color (OTC) field have been studied in recent years [21–33]. The OTC laser field is a superposition of two mutually orthogonal linearly polarized fields having the angular frequencies $r\omega$ and $s\omega$, with r and s integers. The OTC laser fields are used to control the subcycle photoelectron wave packet dynamics by varying the relative phase between the laser-field components [34–36] as well as for velocity map imaging spectroscopy [37]. The OTC-laser-field-induced electron tunneling was considered for negative ions [38] and atoms [39–44]. The temporal double-slit experiment with an OTC field was realized in [45]. Electron holography was discussed in [46,47], while in [48], it was suggested that an OTC field can be used to obtain electrons with a well-defined spin. The ionization of molecules by an OTC laser field was considered in [49–51]. The dissociative double ionization of CO molecules in OTC laser fields was analyzed in [52], while the photoelectron circular dichroism in chiral molecules exposed to the OTC field was investigated in [53].

Both the bicircular field and the OTC field can be considered as special cases of a more general field, the bi-elliptic orthogonal two-color laser (BEOTC) field. This is a superposition of two coplanar elliptically polarized fields with their major polarization axes at right angles to each other. For the component ellipticities $\varepsilon_1 = \varepsilon_2 = 1$ this field reduces to the bicircular field, while for $\varepsilon_1 = \varepsilon_2 = 0$, it becomes the OTC field. In our previous work, we analyzed (H)ATI in bicircular [18] and OTC [33] fields in terms of quantum-orbit theory. Unlike the bicircular and OTC fields, the BEOTC field has an additional degree of freedom, namely the ellipticity of the field, and is valuable to be analyzed in detail. To the best of our knowledge, there are only a few papers considering the HHG [54–57] and HATI [2] processes in the presence of a BEOTC field. In the present paper, we theoretically study the HATI process of inert gas atoms in the presence of a strong BEOTC field. We show that the ionization rate and the cut-off energy strongly depend on the ellipticity of the laser field and the relative phase between two field components. In addition, we find the values of the ellipticity and the relative phase, which maximizes the ionization rate near the cut-off energy. In order to gain a deeper insight into the HATI process, we use the quantum-orbit theory to analyze the obtained results. We find the corresponding saddle-point (SP) solutions of the HATI process in a BEOTC field and present their partial contributions. We also present the most relevant quantum orbits and relate the initial velocity to the ionization yield. The atomic system of units is used throughout the paper.

2. SFA Theory of Strong-Field Ionization

We apply S -matrix theory to find the transition matrix element of the ATI process in a strong laser field. The quantum-mechanical transition amplitude from the ground state, determined by $|\psi_{\ell m}\rangle$ and the ionization potential I_p , to the final Volkov state is described in the SFA, the dipole approximation and in the length gauge by the following integral [5]

$$M_{\mathbf{p}\ell m} = -i \int_{-\infty}^{\infty} dt \langle \mathbf{p} + \mathbf{A}(t) | \mathbf{r} \cdot \mathbf{E}(t) | \psi_{\ell m} \rangle e^{iS(\mathbf{p};t)}, \tag{1}$$

where the ket vector $|\mathbf{p}\rangle$ denotes a plane wave such that $\langle \mathbf{r} | \mathbf{p} \rangle = (2\pi)^{-3/2} e^{i\mathbf{p}\cdot\mathbf{r}}$ and

$$S(\mathbf{p};t) = S_{\mathbf{p}}(t) + I_p t, \quad dS_{\mathbf{p}}(t)/dt = [\mathbf{p} + \mathbf{A}(t)]^2/2. \tag{2}$$

The electric field vector is $\mathbf{E}(t) = -d\mathbf{A}(t)/dt$, while the final electron momentum and kinetic energy are \mathbf{p} and $E_{\mathbf{p}} = \mathbf{p}^2/2$, respectively.

For an infinitely long, periodic laser field with the fundamental frequency ω and the period $T = 2\pi/\omega$, the transition amplitude can be expressed by the T matrix element using the formula

$$M_{\mathbf{p}\ell m} = -2\pi i \sum_n \delta(E_{\mathbf{p}} + I_{\mathbf{p}} + U_{\mathbf{p}} - n\omega) T_{\mathbf{p}\ell m}(n), \tag{3}$$

where $U_{\mathbf{p}} = \int_0^T \mathbf{A}^2(t) dt / (2T)$ is the ponderomotive energy and n is the number of absorbed photons, while the δ function represents the energy conservation law. The corresponding ionization rate with the absorption of n photons can be calculated as follows

$$w_{\mathbf{p}\ell}(n) = 2\pi p \sum_{m=-\ell}^{\ell} |T_{\mathbf{p}\ell m}(n)|^2, \tag{4}$$

where the T -matrix element is a sum of two contributions

$$T_{\mathbf{p}\ell m}(n) = T_{\mathbf{p}\ell m}^{(0)} + T_{\mathbf{p}\ell m}^{(1)}. \tag{5}$$

The first contribution $T_{\mathbf{p}\ell m}^{(0)}$ describes the ATI process and the so-called direct electrons, i.e., electrons that do not interact with the parent ion after ionization and that can be detected directly after ionization. Within the above-mentioned approximations, it is given by the following one-dimensional integral

$$T_{\mathbf{p}\ell m}^{(0)} = \int_0^T \frac{dt}{T} \langle \mathbf{p} + \mathbf{A}(t) | \mathbf{r} \cdot \mathbf{E}(t) | \psi_{\ell m} \rangle e^{iS(\mathbf{p};t)}. \tag{6}$$

On the other hand, the matrix element $T_{\mathbf{p}\ell m}^{(1)}$ is responsible for the HATI process and describes rescattered electrons, i.e., electrons that have an additional interaction with the parent ion before they are detected. It can be calculated using the following two-dimensional integral

$$T_{\mathbf{p}\ell m}^{(1)} = -i \int_0^T \frac{dt}{T} \int_{-\infty}^t dt_0 \left[\frac{2\pi}{i(t-t_0)} \right]^{3/2} \langle \mathbf{p} | V(\mathbf{r}) | \mathbf{k}_{\text{st}} \rangle \times \langle \mathbf{k}_{\text{st}} + \mathbf{A}(t_0) | \mathbf{r} \cdot \mathbf{E}(t_0) | \psi_{\ell m} \rangle e^{i[S_{\mathbf{p}}(t) - S_{\mathbf{k}_{\text{st}}}(t) + S_{\mathbf{k}_{\text{st}}}(t_0) + I_{\mathbf{p}}t_0]}, \tag{7}$$

where

$$\mathbf{k}_{\text{st}} = -\frac{1}{t-t_0} \int_{t_0}^t dt' \mathbf{A}(t') \tag{8}$$

is the stationary momentum and $V(\mathbf{r})$ is the rescattering potential.

In the present paper, we consider only high-energy electrons, i.e., the HATI process using the BEOTC field. The oscillatory integral in the T -matrix element (7) can be computed by numerical integration or by the saddle-point method (SPM). When using the SPM, one must find the saddle points from the stationary conditions $\nabla_{\mathbf{k}} S_{\mathbf{p}i} = \mathbf{0}$, $\partial_{t_0} S_{\mathbf{p}i} = 0$, and $\partial_t S_{\mathbf{p}i} = 0$, where $S_{\mathbf{p}i} = S_{\mathbf{p}}(t) - S_{\mathbf{k}}(t) + S_{\mathbf{k}}(t_0) + I_{\mathbf{p}}t_0$ is the modified action. From the first stationarity condition, we obtain the stationary momentum \mathbf{k}_{st} given by Equation (8) while the other two conditions lead to the following system of nonlinear algebraic equations

$$\frac{1}{2} [\mathbf{k}_{\text{st}} + \mathbf{A}(t_{0s})]^2 = -I_{\mathbf{p}}, \tag{9}$$

$$\frac{1}{2} [\mathbf{k}_{\text{st}} + \mathbf{A}(t_s)]^2 = \frac{1}{2} [\mathbf{p} + \mathbf{A}(t_s)]^2, \tag{10}$$

which represent the energy conservation law at the stationary ionization and rescattering times, respectively.

By choosing the asymptotic wave function as the radial part of the initial state of the valence electron

$$R_{il}(r) \approx Ar^{\nu-1} \exp(-\kappa r), \quad r \gg 1, \tag{11}$$

where $\nu = Z/\kappa$, $\kappa = \sqrt{2I_p}$, and A is a constant tabulated in [58], we can write the $T_{\mathbf{p}\ell m}^{(1)}$ matrix element within the SPM as follows

$$T_{\mathbf{p}\ell m}^{(1),\text{SPM}}(n) = \frac{1}{T} A \pi^2 \kappa^\nu \nu \Gamma(\nu/2) \sum_{\{t_0s, t_s\}} \left(\frac{q_s}{i\kappa}\right)^l Y_{lm}(\hat{\mathbf{q}}_s) \frac{\langle \mathbf{p} | V | \mathbf{k}_{st} \rangle}{[i(t_s - t_0s)]^{3/2}} \times \left(\frac{2i}{S''_{\mathbf{p}i0,s}}\right)^{\frac{\nu+1}{2}} \left(\frac{2i}{S''_{\mathbf{p}i,s}}\right)^{\frac{1}{2}} e^{iS_{\mathbf{p}i,s}}, \tag{12}$$

where $\mathbf{q}_s^2 = [\mathbf{k}_{st} + \mathbf{A}(t_0s)]^2 = -\kappa^2$, $S''_{\mathbf{p}i0,s} = \partial^2 S_{\mathbf{p}i} / \partial t_0^2 = -\mathbf{E}(t_0s) \cdot [\mathbf{k} + \mathbf{A}(t_0s)]$ and $S''_{\mathbf{p}i,s} = \partial^2 S_{\mathbf{p}i} / \partial t^2 = (\mathbf{k}_{st} - \mathbf{p}) \cdot \mathbf{E}(t_s) + [\mathbf{k}_{st} + \mathbf{A}(t_s)]^2 / (t_s - t_0s)$.

3. Numerical Results

We present our numerical results for the HATI process of neon atoms induced by a BEOTC laser field. We calculate the differential ionization rate by solving the integral in the T -matrix element using numerical integration as well as the SPM. The BEOTC field is defined as the sum $\mathbf{E}(t) = \mathbf{E}_1(t) + \mathbf{E}_2(t)$ of two counter-rotating elliptically polarized fields with frequencies $r\omega$ and $s\omega$, given by

$$\mathbf{E}_1(t) = \frac{E_{01}}{\sqrt{1 + \varepsilon_1^2}} [\sin(r\omega t) \hat{\mathbf{e}}_x - \varepsilon_1 \cos(r\omega t) \hat{\mathbf{e}}_y], \tag{13}$$

$$\mathbf{E}_2(t) = \frac{E_{02}}{\sqrt{1 + \varepsilon_2^2}} [\sin(s\omega t + \varphi) \hat{\mathbf{e}}_y - \varepsilon_2 \cos(s\omega t + \varphi) \hat{\mathbf{e}}_x], \tag{14}$$

where ε_1 and ε_2 are the ellipticities of two fields, E_{01} and E_{02} are their amplitudes, and φ is the relative phase between the field components. For $\varepsilon_1 = \varepsilon_2 = 0$, we obtain the OTC field, while for $\varepsilon_1 = \varepsilon_2 = 1$ and $E_{01} = E_{02}$ we obtain the bicircular field. We perform our calculations assuming equal amplitudes and ellipticities of both field components, i.e., $E_{01} = E_{02} \equiv E_0$ and $\varepsilon_1 = \varepsilon_2 \equiv \varepsilon$. In Figure 1 (top panels), we show the polar plots of the electric field vector $\mathbf{E}(t)$ (black solid lines) and the corresponding vector potential $\mathbf{A}(t)$ (red solid lines) in the xy plane for $(r, s) = (1, 2)$ and different values of the ellipticity ε and the phase φ . For $\varepsilon = 0$, we obtain the well-known Lissajous figures, which are characteristic of the OTC field. For $\varepsilon = 1$, both the electric field and the vector potential are rotationally symmetric about an angle of 120° , which is characteristic of the bicircular field.

In the bottom panels of Figure 1, we show the corresponding differential ionization rates of neon atoms exposed to an $\omega - 2\omega$ BEOTC field with equal intensities of two components $I_1 = I_2 = 2 \times 10^{14} \text{ W/cm}^2$, wavelength 1200 nm and emission angle $\theta = 0^\circ$ as a function of the electron energy. The results are obtained by numerical integration of the T -matrix element (7) and by choosing Slater-type orbitals as the initial wave function. Clearly, the HATI spectra depend strongly on the values of ellipticity and relative phase. For $\varphi = 0^\circ$, the spectra do not have a well-defined cutoff and the differential ionization rate decreases continuously with increasing electron energy. For $\varphi = 90^\circ$ and $\varepsilon = 0$, the spectrum has a plateau and a clear cutoff at $8U_p$, while for $\varepsilon = 0.5$ and $\varepsilon = 1$, this cutoff energy decreases to $4U_p$ and $3U_p$, respectively. Furthermore, we can see that the differential ionization rate is about two orders of magnitude higher for $\varphi = 0^\circ$ compared to the spectra obtained for $\varphi = 90^\circ$. Our calculations for other various values of the ellipticity and the relative phase have shown that the differential ionization rate and the cutoff energy change a lot with changing the values of these two laser field parameters.

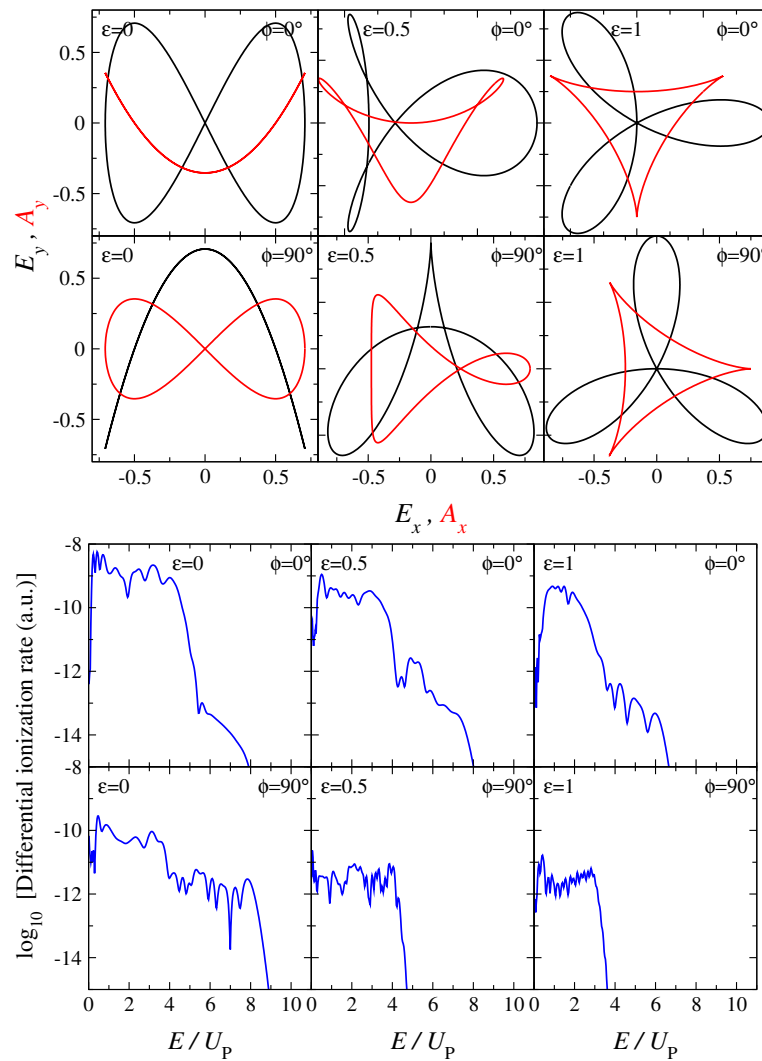


Figure 1. Top panels: electric-field vector $E(t)$ (black lines), and the corresponding vector potential $A(t)$ (red lines) of the $\omega - 2\omega$ BEOTC laser field for various values of ellipticity and relative phase. Bottom panels: logarithm of the differential ionization rate (in a.u.) of neon atoms ionized by a $\omega - 2\omega$ BEOTC field with equal intensities of two components $I_1 = I_2 = 2 \times 10^{14} \text{ W/cm}^2$, wavelength 1200 nm and emission angle $\theta = 0^\circ$, plotted as a function of the electron energy (in U_p) for various values of ellipticity and relative phase.

From the previous analysis, we conclude that it is possible to choose laser field parameters to obtain a high ionization rate but low cutoff energy and vice versa. Therefore, we want to find the values of ellipticity and relative phase of a BEOTC field that maximize the differential ionization rate for a fixed value of the energy that is close to the cut-off energy. This is also of particular interest for the HHG process, because one could find the optimal laser field parameters for which the harmonic rate is maximal for the highest possible frequency of the obtained harmonic. We choose the value of the final electron energy E_p to be $9U_p$, where the ponderomotive energy for the BEOTC field is given by $U_p = \frac{1}{4}(A_{01}^2 + A_{02}^2)$, with $A_{01} = E_{01}/r\omega$ and $A_{02} = E_{02}/s\omega$, and plot the differential ionization rate as a function of ellipticity and relative phase. Such a color false plot is shown in Figure 2. We can see that there is a global maximum of the differential ionization rate for the relative phase close to $\varphi = 240^\circ$ and the ellipticity close to $\epsilon = 0.3$. Now, we can find the maximum of the differential ionization rate numerically, using these values of φ and ϵ as an initial guess. We performed an optimization procedure within the multidimensional downhill simplex method [59]. Starting from the initial simplex, which is an N -dimensional geometric figure consisting of $N + 1$ points and all their connecting line segments, the downhill simplex

method performs a series of reflections, each reflection moving from a point on the simplex through the opposite side of the simplex to a point where the function is smaller. Using this method, we found that for $\varphi = 243.9^\circ$ and $\varepsilon = 0.272$ the ionization rate is highest at the energy $E_p = 9U_p$. The corresponding electron energy spectrum, electric field, and vector potential are shown in Figure 3 for these laser field parameters.

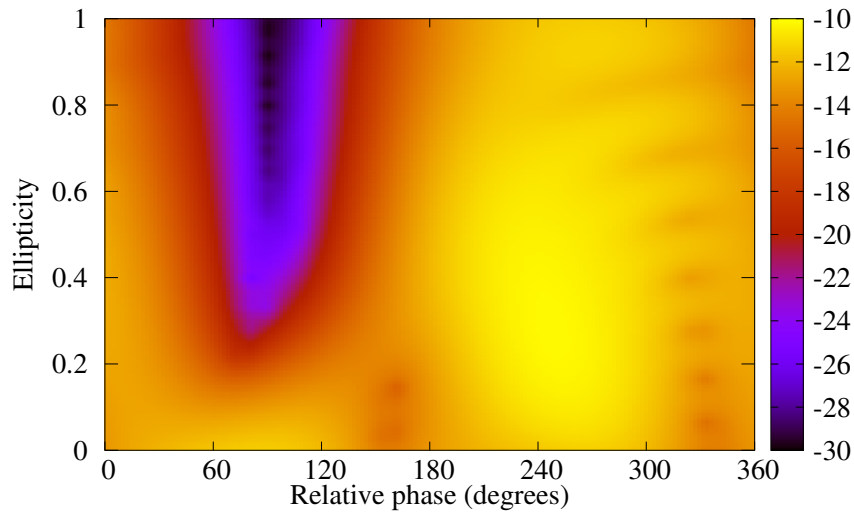


Figure 2. Logarithm of the differential ionization rate (in a.u.) of Ne atoms presented in false colors as a function of laser field ellipticity and the relative phase between field components for ionization by the $\omega - 2\omega$ BEOC field with the same field parameters as in Figure 1. The results are obtained via numerical integration of the SFA T -matrix element.

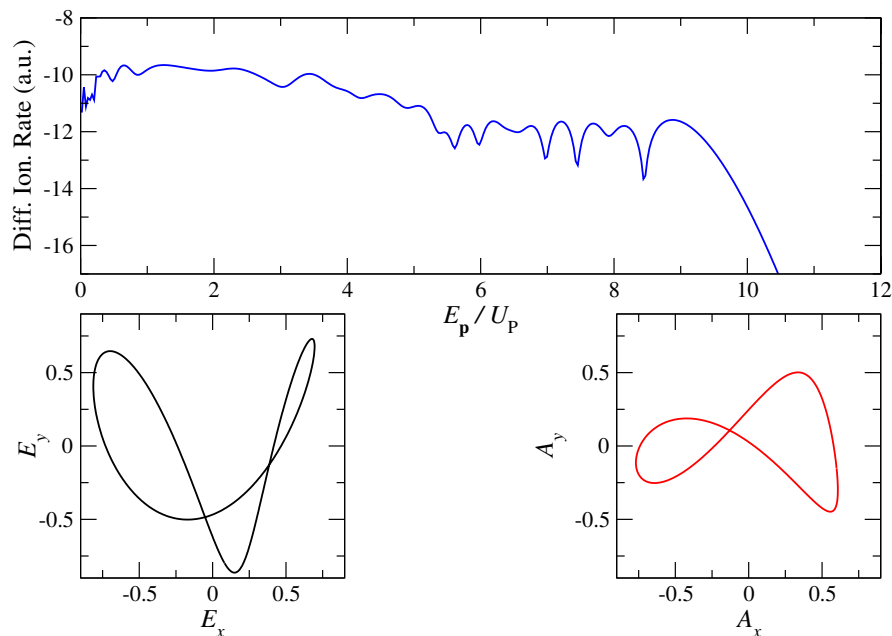


Figure 3. Top panel: logarithm of the differential ionization rate (in a.u.) of neon atoms ionized by an $\omega - 2\omega$ BEOC field for $\varphi = 243.9^\circ$ and $\varepsilon = 0.272$ and the same laser field parameters as in Figure 1. Bottom left (right): electric field $\mathbf{E}(t)$ (vector potential $\mathbf{A}(t)$) of the $\omega - 2\omega$ BEOC laser field for $\varphi = 243.9^\circ$ and $\varepsilon = 0.272$ and same field parameters as in Figure 1.

4. Quantum-Orbit Analysis

In this section, we present the quantum-orbit analysis for the HATI process of Ne atoms exposed to the $\omega - 2\omega$ BEOC field. To explain the results of the previous section, we use the SPM to find the most relevant SP contributions for the laser field parameters

that maximize the ionization rate at $9U_p$, i.e., for $\varphi = 243.9^\circ$ and $\varepsilon = 0.272$. First, we numerically solve the system of nonlinear algebraic Equations (9) and (10) to find the stationary ionization and rescattering times. Since the number of solutions for a periodic laser field is infinite, we need to classify these SP solutions. We use the same classification of the solutions relevant to the HATI spectra that was introduced previously for linear, bicircular, and OTC laser fields. Furthermore, we consider only the high energy part of the spectra, for which the so-called backward-scattering solutions, classified by a multiple index (α, β, m) , are relevant. The approximate length of the travel time in multiples of the laser period is given by the index m , which is defined as $m = [\text{Re}(t_s - t_{0s})]/T$. Similarly to the OTC field, there are $2s$ pairs of backward-scattering solutions within one period of the $r\omega - s\omega$ BEOTC field. For a fixed value of m , each pair of solutions within a period is indexed by $\beta \in (1, 2, 3, \dots, 2s)$. Finally, for fixed values of β and m , each pair of solutions consists of two orbits with slightly different travel times. The longer orbit ($\alpha = -1$) and the shorter orbit ($\alpha = +1$) are distinguished by the index α .

The saddle point solutions $\{t_0, t_r\}$, classified by the above notation (α, β, m) , are shown in Figure 4. From the upper panel of Figure 4 it can be seen that there are four pairs of solutions within one optical cycle, i.e., $2s$ pairs of solutions, which corresponds to the previously found number of solutions for an $r\omega - s\omega$ BEOTC field. The SP solution, denoted $(\beta, m) = (0, 0)$, is the only forward-scattering solution that does not contribute significantly to the high-energy part of the spectrum. The backward-scattering solutions are shown in the left (right) bottom panel of Figure 4 for even (odd) values of the index β . It is evident that each pair of solutions converges as the electron energy increases. At the cutoff energy, the solution pairs merge while one solution diverges.

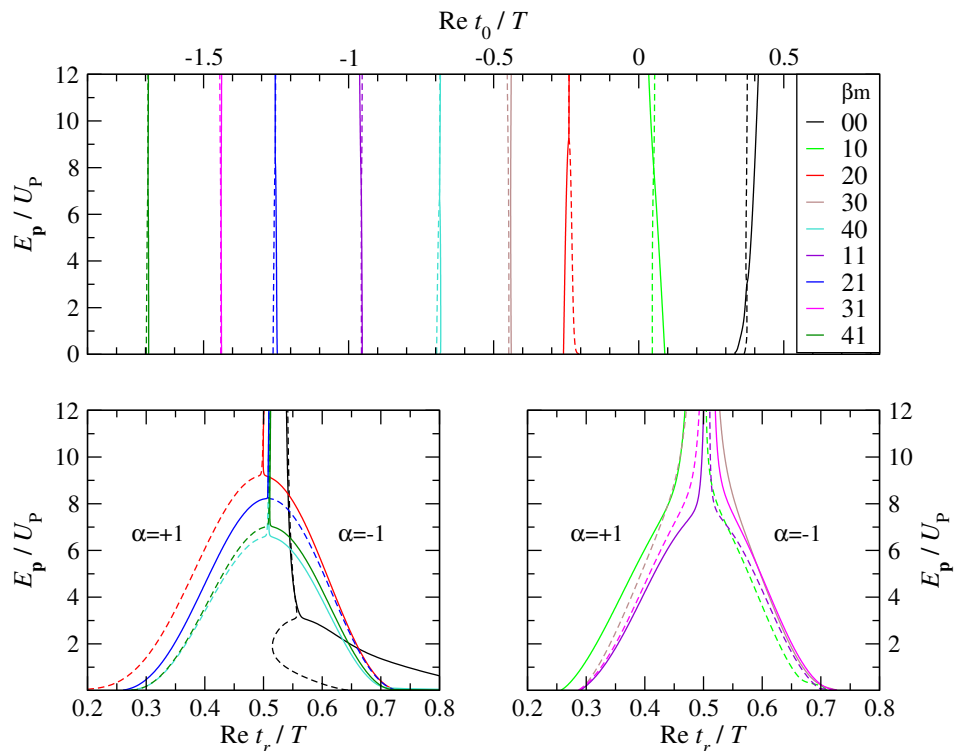


Figure 4. Solutions of the system of the saddle-point Equations (9) and (10) for Ne atoms, emission angle $\theta = 0^\circ$, and the $\omega - 2\omega$ BEOTC laser field with the same field parameters as in Figure 3. For each of the plotted solutions, the electron energy E_p is presented as a function of the real part of the electron ionization time $\text{Re } t_0$ (**top**) and the real part of the rescattering time $\text{Re } t_r$ for even (**bottom left**) and odd (**bottom right**) values of index β . Only the backward-scattering solutions with $m = 0, 1$ and one pair of the forward-scattering solutions denoted by $(\alpha, \beta, m) = (\pm 1, 0, 0)$ are presented. The solutions whose contribution should be discarded after the cutoff are represented by the dashed lines.

As shown earlier [33], solutions characterized by even values of the parameter β have a well-defined cut-off energy and make a substantial contribution to the ionization rate. Conversely, solutions associated with odd values of the parameter β have negligible contributions. It can be observed that the solution pair indexed as $(\beta, m) = (2, 0)$ has a well-defined cutoff at the energy of $9U_p$, and we expect this particular solution pair to have the highest contribution at this energy. In addition, we expect the solution pairs $(\beta, m) = (2, 1)$, $(\beta, m) = (4, 0)$ and $(\beta, m) = (4, 1)$ to contribute significantly to the overall ionization rate, albeit at lower energies.

Using Equation (12), we evaluate the individual contributions of each solution and sum them to the total ionization rate. Figure 5 shows the partial contributions of all relevant SP solutions, as well as the differential ionization rate obtained by SPM (represented by the line labeled Σ in the legend) and numerical integration (represented by the line labeled "NI" in the legend). As mentioned above, one of the two solutions within each pair (either $\alpha = +1$ or $\alpha = -1$) diverges beyond the cut-off energy and should be disregarded. This divergent solution is shown by a dashed line. The agreement between the results obtained using numerical integration and those obtained using the SPM method is very good, especially for the high-energy part of the spectrum. The low-energy part of the spectrum is mainly determined by the forward-scattering solutions, which are not of interest in this paper. As expected, we see that the solution pair $(\beta, m) = (2, 0)$ is dominant throughout the plateau. The contributions from other SP solutions are at least one order of magnitude smaller. However, due to constructive interference, they also contribute to the high energy part of the spectra and create a distinctive oscillation pattern. It is worth noting that for energies close to the cut-off energy of each SP solution, the uniform approximation should be used instead of the SP approximation.

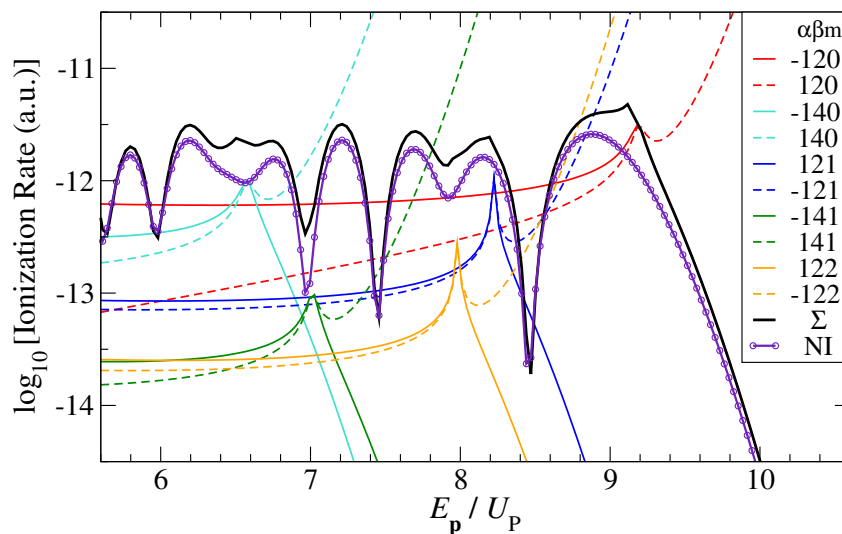


Figure 5. Comparison of the differential ionization rates as a function of electron energy (in units of U_p) for the same parameters as in Figure 3. The results obtained via numerical integration are shown by an indigo dashed line, while the results obtained as a coherent sum of the contributions of the saddle-point solutions are shown by a solid black line. The partial ionization rates for each of the solutions (α, β, m) are presented and identified by their colors, as explained in the legend. The contributions of the divergent solutions are neglected after the corresponding cutoff values.

To better understand the HATI process induced by the BEOTC field, we use the concept of quantum orbits, which are defined as solutions of the classical Newton equation for the electron in the presence of the laser field, but for complex ionization and rescattering times. We define the electron orbits as the real part of $\mathbf{r}(t)$ for real t , with

$$\mathbf{r}(t) = \begin{cases} (t - t_0)\mathbf{k}_{st} + \boldsymbol{\alpha}(t) - \boldsymbol{\alpha}(t_0), & \text{Re}(t_0) \leq t \leq \text{Re}(t_r), \\ (t - t_r)\mathbf{p} + \boldsymbol{\alpha}(t) - \boldsymbol{\alpha}(t_r), & t > \text{Re}(t_r), \end{cases} \quad (15)$$

while the corresponding electron velocities are defined as the real part of $\mathbf{v}(t)$, where

$$\mathbf{v}(t) = \frac{d\mathbf{r}(t)}{dt} = \begin{cases} \mathbf{k}_{st} + \mathbf{A}(t), & \text{Re}(t_0) \leq t \leq \text{Re}(t_r), \\ \mathbf{p} + \mathbf{A}(t), & t > \text{Re}(t_r). \end{cases} \quad (16)$$

In Figure 6, we show three electron trajectories (left panel) that make the largest contribution to the total ionization rate, as well as their velocities (right panel). The trajectories and velocities are plotted for solutions indexed as $(\alpha, \beta, m) = (-1, 2, 0)$, $(-1, 4, 0)$, and $(1, 2, 1)$ with the corresponding cutoff energies $9U_p$, $6.4U_p$, and $8.1U_p$, respectively. It is evident that the electrons emerge from a distance of a few atomic units from the origin. This is attributed to the fact that the liberated electrons tunnel through a potential barrier formed by the atomic and external laser field potentials. On the other hand, the scattering process takes place at the position of the atomic nucleus, and we see that all three backscattering trajectories scatter at relatively large angles. In the middle panel of Figure 6, we plot the electric field and the vector potential for the laser field parameters that maximize the ionization rate at $9U_p$ and show with circles (stars) the value of the electric field and the vector potential at the ionization (rescattering) times. Similar to HATI with linearly polarized and OTC fields, we can conclude that ionization occurs when the electric field intensity is close to its maximum value, while electron rescattering occurs when the vector potential intensity is at its maximum. It is also evident that the electron trajectories are similar to the shape of the electric field during one period of the laser field, while the velocities undergo a similar change to that of the vector potential throughout the period of the laser field.

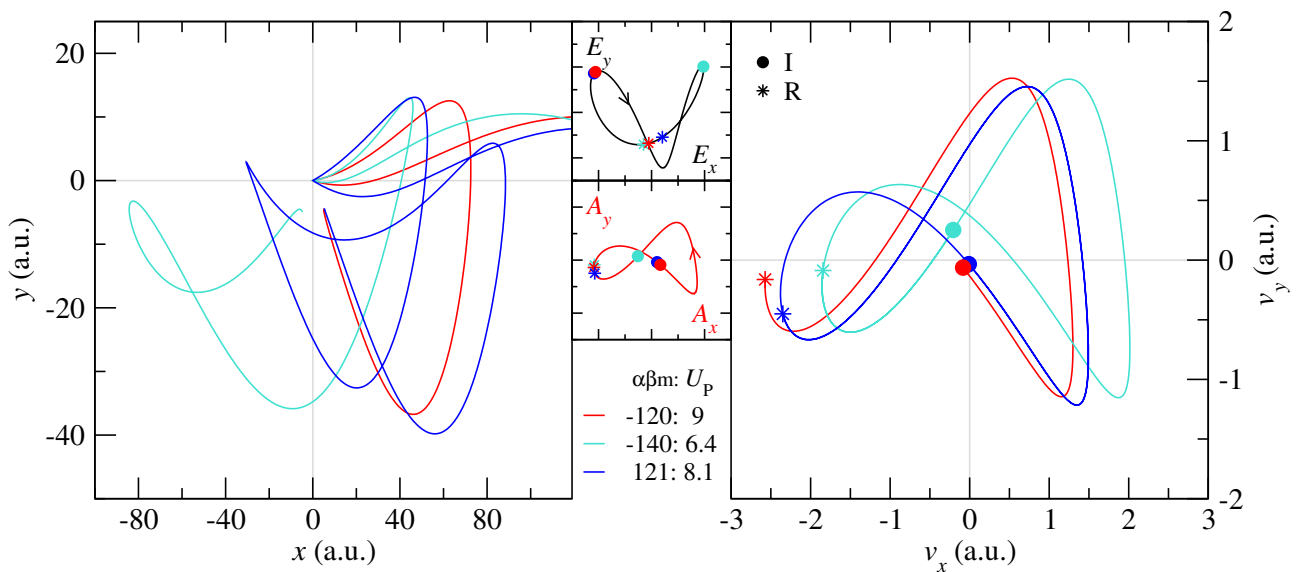


Figure 6. Electron trajectories (left) and velocities (right) for some of the quantum-orbit solutions presented in Figure 4. The value of the velocity at the ionization (rescattering) times is represented by circles (stars). The electron energies for the presented solutions are $9U_p$, $8.1U_p$, and $6.4U_p$ for the solutions $(\beta, m) = (2, 0)$, $(2, 1)$, and $(4, 0)$, respectively. The electric field $\mathbf{E}(t)$ and the vector potential $\mathbf{A}(t)$ are plotted in the middle panel for the same laser field parameters as in Figure 3. Circles (stars) denote the values of the electric field and vector potential at the ionization (rescattering) time.

In the right panel of Figure 6, we show the velocity change of the three most relevant trajectories between the ionization and rescattering times. It can be seen that, unlike the other trajectories, the initial velocity of the trajectories indexed by $(\alpha, \beta, m) = (-1, 2, 0)$ and $(-1, 4, 0)$ is approximately zero. Considering that the ionization rate decreases exponentially with the initial velocity, we conclude that these trajectories would make the highest contribution to the differential ionization rate. This inference is consistent with the

results shown in Figure 5. In addition, these two trajectories have the highest velocity at the rescattering time and therefore, they have the dominant contribution at the cutoff energy.

5. Conclusions

Atomic and molecular processes induced by strong tailored laser fields are of present interest in strong-field physics and attoscience communities. In our contribution, we analyzed high-order above-threshold ionization using such fields. In particular, we studied HATI of noble-gas atoms by bi-elliptical orthogonal two-color laser field, with a particular emphasis on two special cases: the OTC field, for which the ellipticities of the field components are zero, and the bicircular field with equal counter-rotating component intensities and ellipticities. For this purpose, we applied the *S*-matrix theory and used the strong-field approximation. The corresponding HATI rescattering amplitude was calculated using numerical integration. Furthermore, we applied an optimization procedure to find the optimal (i.e., highest) ionization rate for a given photoelectron energy.

In order to obtain a better physical insight into the obtained results, we used the quantum-orbit theory. We classified the rescattering saddle-point solutions and found those solutions that give the main contribution to the ionization rate. In addition, we visualized our quantum-orbit results by presenting the electron trajectories and velocities for dominant quantum-orbit solutions.

Our results can be used to understand and optimize the high-energy photoelectron spectra in strong-field ionization by tailored fields. In this way, we can achieve better insight into atomic and molecular structures, and, furthermore, our findings can stimulate the investigation of processes induced by the BEOTC field.

Author Contributions: Investigation, A.S.J., E.H. and D.B.M.; software, A.S.J. and E.H.; writing—original draft, E.H.; writing—review and editing, D.B.M. All authors have read and agreed to the published version of the manuscript.

Funding: This research received no external funding.

Acknowledgments: We acknowledge support by the Ministry of Science, Higher Education and Youth, Canton Sarajevo, Bosnia and Herzegovina.

Conflicts of Interest: The authors declare no conflict of interest.

References

1. Heinrich, T.; Taucer, M.; Kfir, O.; Corcum, P.B.; Staudte, A.; Ropers, C.; Sivis, M. Chiral high-harmonic generation and spectroscopy on solid surfaces using polarization-tailored strong fields. *Nat. Commun.* **2021**, *12*, 3723.
2. Becker, W.; Milošević, D.B. Elliptic dichroism in strong-field ionization of atoms subjected to tailored laser fields. *Phys. Chem. Chem. Phys.* **2022**, *24*, 7014–7027. [[CrossRef](#)]
3. Kfir, O.; Grychtol, P.; Turgut, E.; Knut, R.; Zusin, D.; Popmintchev, D.; Popmintchev, T.; Nembach, H.; Shaw, J.M.; Fleischer, A.; et al. Generation of bright phase-matched circularly-polarized extreme ultraviolet high harmonics. *Nat. Photonics* **2015**, *9*, 99–105. [[CrossRef](#)]
4. Jiménez-Galán, Á.; Silva, R.E.F.; Smirnova, O.; Ivanov, M. Lightwave control of topological properties in 2D materials for sub-cycle and non-resonant valley manipulation. *Nat. Photonics* **2020**, *14*, 728–732. [[CrossRef](#)]
5. Becker, W.; Goreslavski, S.P.; Milošević, D.B.; Paulus, G.G. The plateau in above-threshold ionization: The keystone of rescattering physics. *J. Phys. B* **2018**, *51*, 162002. [[CrossRef](#)]
6. Kohler, M.; Pfeifer, T.; Hatsagortsyan, K.; Keitel, C. Frontiers of Atomic High-Harmonic Generation. *Adv. At. Mol. Opt. Phys.* **2012**, *61*, 159–208.
7. Corkum, P.B. Plasma perspective on strong field multiphoton ionization. *Phys. Rev. Lett.* **1993**, *71*, 1994–1997. [[CrossRef](#)]
8. Schafer, K.J.; Yang, B.; DiMauro, L.F.; Kulander, K.C. Above threshold ionization beyond the high harmonic cutoff. *Phys. Rev. Lett.* **1993**, *70*, 1599–1602. [[CrossRef](#)]
9. Paulus, G.G.; Becker, W.; Nicklich, W.; Walther, H. Rescattering effects in above-threshold ionization: A classical model. *J. Phys. B* **1994**, *27*, L703–L708. [[CrossRef](#)]
10. Eichmann, H.; Egbert, A.; Nolte, S.; Momma, C.; Wellegehausen, B.; Becker, W.; Long, S.; McIver, J.K. Polarization-dependent high-order two-color mixing. *Phys. Rev. A* **1995**, *51*, R3414–R3417.
11. Long, S.; Becker, W.; McIver, J.K. Model calculations of polarization-dependent two-color high-harmonic generation. *Phys. Rev. A* **1995**, *52*, 2262–2278. [[CrossRef](#)]

12. Milošević, D.B.; Becker, W.; Kopold, R. Generation of circularly polarized high-order harmonics by two-color coplanar field mixing. *Phys. Rev. A* **2000**, *61*, 063403. [[CrossRef](#)]
13. Fleischer, A.; Kfir, O.; Diskin, T.; Sidorenko, P.; Cohen, O. Spin angular momentum and tunable polarization in high-harmonic generation. *Nat. Photonics* **2014**, *8*, 543–549. [[CrossRef](#)]
14. Kramo, A.; Hasović, E.; Milošević, D.B.; Becker, W. Above-threshold detachment by a two-color bicircular laser field. *Las. Phys. Lett.* **2007**, *4*, 279–286. [[CrossRef](#)]
15. Mancuso, C.A.; Hickstein, D.D.; Dorney, K.M.; Ellis, J.L.; Hasović, E.; Knut, R.; Grychtol, P.; Gentry, C.; Gopalakrishnan, M.; Zusin, D.; et al. Controlling electron-ion rescattering in two-color circularly polarized femtosecond laser fields. *Phys. Rev. A* **2016**, *93*, 053406. [[CrossRef](#)]
16. Eckart, S.; Richter, M.; Kunitski, M.; Hartung, A.; Rist, J.; Henrichs, K.; Schlott, N.; Kang, H.; Bauer, T.; Sann, H.; et al. Nonsequential double ionization by counterrotating circularly polarized two-color laser fields. *Phys. Rev. Lett.* **2016**, *117*, 133202. [[CrossRef](#)]
17. Korajac, A.; Habibović, D.; Čerkić, A.; Busuladžić, M.; Milošević, D.B. Electron-atom potential scattering assisted by a bichromatic elliptically polarized laser field. *Eur. Phys. J. D* **2017**, *71*, 251. [[CrossRef](#)]
18. Milošević, D.B. Possibility of introducing spin into attosecond with spin-polarized electrons produced by a bichromatic circularly polarized laser field. *Phys. Rev. A* **2016**, *93*, 051402. [[CrossRef](#)]
19. Baykusheva, D.; Ahsan, M.S.; Lin, N.; Wörner, H.J. Bicircular high-harmonic spectroscopy reveals dynamical symmetries of atoms and molecules. *Phys. Rev. Lett.* **2016**, *116*, 123001. [[CrossRef](#)]
20. Chen, Z.Y. Spectral control of high harmonics from relativistic plasmas using bicircular fields. *Phys. Rev. E* **2018**, *97*, 043202. [[CrossRef](#)]
21. Perry, M.D.; Crane, J.K. High-order harmonic emission from mixed fields. *Phys. Rev. A* **1993**, *48*, R4051. [[CrossRef](#)]
22. Kim, I.J.; Kim, C.M.; Kim, H.T.; Lee, G.H.; Lee, Y.S.; Park, J.Y.; Cho, D.J.; Nam, C.H. Highly efficient high-harmonic generation in an orthogonally polarized two-color laser field. *Phys. Rev. Lett.* **2005**, *94*, 243901. [[CrossRef](#)]
23. Brugnera, L.; Hoffmann, D.J.; Siegel, T.; Frank, F.; Zair, A.; Tisch, J.W.; Marangos, J.P. Trajectory selection in high harmonic generation by controlling the phase between orthogonal two-color fields. *Phys. Rev. Lett.* **2011**, *107*, 153902. [[CrossRef](#)]
24. Niikura, H.; Dudovich, N.; Villeneuve, D.M.; Corkum, P.B. Mapping molecular orbital symmetry on high-order harmonic generation spectrum using two-color laser fields. *Phys. Rev. Lett.* **2010**, *105*, 053003. [[CrossRef](#)]
25. Sarantseva, T.S.; Frolov, M.V.; Manakov, N.L.; Ivanov, M.Y.; Starace, A.F. Harmonic generation spectroscopy with a two-colour laser field having orthogonal linear polarizations. *J. Phys. B* **2013**, *46*, 231001. [[CrossRef](#)]
26. Zhai, C.; Zhang, X.; Zhu, X.; He, L.; Zhang, Y.; Wang, B.; Zhang, Q.; Lan, P.; Lu, P. Single-shot molecular orbital tomography with orthogonal two-color fields. *Opt. Express* **2018**, *26*, 2775–2784. [[CrossRef](#)] [[PubMed](#)]
27. Habibović, D.; Gazibegović-Busuladžić, A.; Busuladžić, M.; Čerkić, A.; Milošević, D.B. Strong-field ionization of homonuclear diatomic molecules using orthogonally polarized two-color laser fields. *Phys. Rev. A* **2020**, *102*, 023111. [[CrossRef](#)]
28. Fu, T.; Guo, F.; Wang, J.; Chen, J.; Yang, Y. Waveform Modulation of High-Order Harmonics Generated from an Atom Irradiated by a Laser Pulse and a Weak Orthogonal Electrostatic Field. *Symmetry* **2023**, *15*, 901. [[CrossRef](#)]
29. Zhang, C.; Yao, J.; Umran, F.A.; Ni, J.; Zeng, B.; Li, G.; Lin, D. Enhanced narrow-bandwidth emission during high-order harmonic generation from aligned molecules. *Opt. Express* **2013**, *21*, 3259–3264. [[CrossRef](#)] [[PubMed](#)]
30. Gong, X.; Wei, P.; Guan, Z.; Jiao, Z.H.; Wang, G.L.; Hu, S.; Zhao, S.F. Generation of elliptically polarized isolated attosecond pulses from N₂ and O₂ molecules in orthogonal few-cycle two-color fields. *Results Phys.* **2023**, *45*, 106215. [[CrossRef](#)]
31. Sanari, Y.; Oboe, T.; Kanemitsu, Y.; Hirori, H. Modifying angular and polarization selection rules of high-order harmonics by controlling electron trajectories in k-space. *Nat. Commun.* **2020**, *11*, 3069. [[CrossRef](#)] [[PubMed](#)]
32. Popova, M.M.; Gryzlova, E.V.; Kiselev, M.D.; Grum-Grzhimailo, A.N. Symmetry violation in bichromatic ionization by a free-electron laser: Photoelectron angular distribution and spin polarization. *Symmetry* **2021**, *13*, 1015. [[CrossRef](#)]
33. Jašarević, A.; Hasović, E.; Milošević, D.B. Ionization by a strong orthogonal two-color laser field: A quantum-orbit-theory approach. *Eur. Phys. J. D* **2022**, *76*, 240–257. [[CrossRef](#)]
34. Kitzler, M.; O’Keeffe, K.; Lezius, M. Attosecond control of electronic motion using light wave synthesis. *J. Mod. Opt.* **2006**, *53*, 57–66. [[CrossRef](#)]
35. Zhou, Y.; Huang, C.; Liao, Q.; Hong, W.; Lu, P. Control the revisit time of the electron wave packet. *Opt. Lett.* **2011**, *36*, 2758–2760. [[CrossRef](#)]
36. Xie, X. Two-Dimensional Attosecond Electron Wave-Packet Interferometry. *Phys. Rev. Lett.* **2015**, *114*, 173003. [[CrossRef](#)]
37. Würzler, D.; Eicke, N.; Möller, M.; Seipt, D.; Sayler, A.M.; Fritzsche, S.; Lein, M.; Paulus, G.G. Velocity map imaging of scattering dynamics in orthogonal two-color fields. *J. Phys. B* **2017**, *51*, 015001. [[CrossRef](#)]
38. Chen, J.H.; Han, M.; Xiao, X.R.; Peng, L.Y.; Liu, Y. Atomic-orbital-dependent photoelectron momentum distributions for F[−] ions by orthogonal two-color laser fields. *Phys. Rev. A* **2018**, *98*, 033403. [[CrossRef](#)]
39. Geng, J.W.; Xiong, W.H.; Xiao, X.R.; Peng, L.Y.; Gong, Q. Nonadiabatic Electron Dynamics in Orthogonal TwoColor Laser Fields with Comparable Intensities. *Phys. Rev. Lett.* **2015**, *115*, 193001. [[CrossRef](#)]
40. Henkel, J.; Lein, M. Analysis of electron trajectories with two-color strong-field ionization. *Phys. Rev. A* **2015**, *92*, 013422. [[CrossRef](#)]

41. Li, Y.; Zhou, Y.; He, M.; Li, M.; Lu, P. Identifying backwardscattering photoelectron hologram with orthogonal two-color laser fields. *Opt. Express* **2016**, *24*, 23697. [[CrossRef](#)]
42. Han, M.; Ge, P.; Shao, Y.; Liu, M.M.; Deng, Y.; Wu, C.; Gong, Q.; Liu, Y. Revealing the Sub-Barrier Phase using a Spatiotemporal Interferometer with Orthogonal Two-Color Laser Fields of Comparable Intensity. *Phys. Rev. Lett.* **2017**, *119*, 073201. [[CrossRef](#)] [[PubMed](#)]
43. Xie, W.; Li, M.; Luo, S.; He, M.; Liu, K.; Zhang, Q.; Zhou, Y.; Lu, P. Nonadiabaticity-induced ionization time shift in strong-field tunneling ionization. *Phys. Rev. A* **2019**, *100*, 023414. [[CrossRef](#)]
44. Han, M.; Ge, P.; Fang, Y.; Deng, Y.; Wu, C.; Gong, Q.; Liu, Y. Quantum effect of laser-induced rescattering from the tunneling barrier. *Phys. Rev. A* **2019**, *99*, 023418. [[CrossRef](#)]
45. Richter, M.; Kunitski, M.; Schöffler, M.; Jahnke, T.; Schmidt, L.P.; Li, M.; Liu, Y.; Dörner, R. Streaking temporal double-slit interference by an orthogonal two-color laser field. *Phys. Rev. Lett.* **2015**, *114*, 143001. [[CrossRef](#)] [[PubMed](#)]
46. He, M.; Li, Y.; Zhou, Y.; Li, M.; Lu, P. Temporal and spatial manipulation of the recolliding wave packet in strong-field photoelectron holography. *Phys. Rev. Lett.* **2016**, *93*, 033406. [[CrossRef](#)]
47. Tan, J.; Zhou, Y.; He, M.; Ke, Q.; Liang, J.; Li, Y.; Li, M.; Lu, P. Time-resolving tunneling ionization via strong-field photoelectron holography. *Phys. Rev. A* **2019**, *99*, 033402. [[CrossRef](#)]
48. Han, M.; Ge, P.; Liu, M.M.; Gong, Q.; Liu, Y. Spatially and temporally controlling electron spin polarization in strong-field ionization using orthogonal two-color laser fields. *Phys. Rev. A* **2019**, *99*, 023404. [[CrossRef](#)]
49. Yuan, K.J.; Chelkowski, S.; Bandrauk, A.D. Molecular photoelectron momentum distributions by intense orthogonally polarized attosecond ultraviolet laser pulses. *Chem. Phys. Lett.* **2015**, *638*, 173–178. [[CrossRef](#)]
50. Gao, F.; Chen, Y.J.; Xin, G.G.; Liu, J.; Fu, L.B. Distilling two-center-interference information during tunneling of aligned molecules with orthogonally polarized two-color laser fields. *Phys. Rev. A* **2017**, *96*, 063414. [[CrossRef](#)]
51. Liu, M.M.; Han, M.; Ge, P.; He, C.; Gong, Q.; Liu, Y. Strong-field ionization of diatomic molecules in orthogonally polarized two-color fields. *Phys. Rev. A* **2018**, *97*, 063416. [[CrossRef](#)]
52. Song, Q.; Lu, P.; Gong, X.; Ji, Q.; Lin, K.; Zhang, W.; Ma, J.; Zeng, H.; Wu, J. Dissociative double ionization of CO in orthogonal two-color laser fields. *Phys. Rev. A* **2017**, *95*, 013406. [[CrossRef](#)]
53. Demekhin, P.V.; Artemyev, A.N.; Kastner, A.; Baumert, T. Photoelectron Circular Dichroism with Two Overlapping Laser Pulses of Carrier Frequencies ω and 2ω Linearly Polarized in Two Mutually Orthogonal Directions. *Phys. Rev. Lett.* **2018**, *121*, 253201. [[CrossRef](#)] [[PubMed](#)]
54. Bordo, E.; Neufeld, O.; Kfir, O.; Fleischer, A.; Cohen, O. Spectroscopy of atomic orbital sizes using bi-elliptical high-order harmonic generation. *Phys. Rev. A* **2019**, *100*, 043419. [[CrossRef](#)]
55. Bordo, E.; Kfir, O.; Zayko, S.; Neufeld, O.; Fleischer, A.; Ropers, C.; Cohen, O. Interlocked attosecond pulse trains in slightly bi-elliptical high harmonic generation. *J. Phys. Photonics* **2020**, *2*, 034005. [[CrossRef](#)]
56. Zayko, S.; Kfir, O.; Bordo, E.; Fleischer, A.; Cohen, O.; Ropers, C. A dynamical symmetry triad in high-harmonic generation revealed by attosecond recollision control. *New J. Phys.* **2020**, *22*, 053017. [[CrossRef](#)]
57. Milošević, D.B.; Becker, W. High-order harmonic generation by bi-elliptical orthogonally polarized two-color fields. *Phys. Rev. A* **2020**, *102*, 023107. [[CrossRef](#)]
58. Radzig A.A.; Smirnov, B.M. *Reference Data on Atoms, Molecules and Ions*; Springer: Berlin, Germany, 1985.
59. Press, W.H.; Teukolsky, S.A.; Vetterling, W.T.; Flannery, B.P. *Numerical Recipes 3rd Edition: The Art of Scientific Computing*; Cambridge University Press: Cambridge, UK, 2007.

Disclaimer/Publisher's Note: The statements, opinions and data contained in all publications are solely those of the individual author(s) and contributor(s) and not of MDPI and/or the editor(s). MDPI and/or the editor(s) disclaim responsibility for any injury to people or property resulting from any ideas, methods, instructions or products referred to in the content.